Incorporating redox-sensitive nanogels into bioabsorbable nanofibrous membrane to acquire ROS-balance capacity for skin regeneration

Shihao Zhang [a,1], Yamin Li [d,1], Xiaofeng Qiu [a,1], Anqi Jiao [a], Wei Luo [a], Xiajie Lin [a], Xiaohui Zhang [a], Zeren Zhang [a], Jiachan Hong [a], Peihao Cai [a], Yuhong Zhang [e], Yan Wu [c,*], Jie Gao [b,**], Changsheng Liu [a,***], Yulin Li [a,e,****]

[a] *The Key Laboratory for Ultrafine Materials of Ministry of Education, State Key Laboratory of Bioreactor Engineering, Engineering Research Center for Biomedical Materials of Ministry of Education, School of Materials Science and Engineering, East China University of Science and Technology, Shanghai, 200237, China*
[b] *Institute of Translational Medicine, Shanghai University, Shanghai, 200444, China*
[c] *Heilongjiang Key Laboratory of Anti-fibrosis Biotherapy, Mudanjiang Medical University, Mudanjiang, 157011, China*
[d] *Shanghai Jiaotong University Affiliated Sixth People's Hospital, Shanghai, 200233, China*
[e] *Hubei Collaborative Innovation Center for Advanced Organic Chemical Materials, Ministry of Education Key Laboratory for the Synthesis and Application of Organic Functional Molecules, College of Chemistry and Chemical Engineering, Hubei University, Wuhan, 430062, China*

ARTICLE INFO

ABSTRACT

Facing the high incidence of skin diseases, it is urgent to develop functional materials with high bioactivity for wound healing, where reactive oxygen species (ROS) play an important role in the wound healing process mainly *via* adjustment of immune response and neovasculation. In this study, we developed a kind of bioabsorbable materials with ROS-mediation capacity for skin disease therapy. Firstly, redox-sensitive poly(N-iso-propylacrylamide-acrylic acid) (PNA) nanogels were synthesized by radical emulsion polymerization method using a disulfide molecule as crosslinker. The resulting nanogels were then incorporated into the nanofibrous membrane of poly(L-lactic acid) (PLLA) *via* airbrushing approach to offer bioabsorbable membrane with redox-sensitive ROS-balance capacity. *In vitro* biological evaluation indicated that the PNA-contained bioabsorbable membrane improved cell adhesion and proliferation compared to the native PLLA membrane. *In vivo* study using mouse wound skin model demonstrated that PNA-doped nanofibrous membranes could promote the wound healing process, where the disulfide bonds in them were able to adjust the ROS level in the wound skin for mediation of redox potential to achieve higher wound healing efficacy.

1. Introduction

As the largest organ of organism, skin plays an essential role in adjustment of the normal biological activities of human body (e.g., infection prevention, nutrient and waste exchange, hydration and temperature regulation) [1–3]. Also, the maintenance of skin integrity is a necessity for insuring the homeostasis of human body. However, major skin injuries from trauma or illness may dis-functionalize its primary defense capacity, resulting in serious infections or disabilities to endanger the quality of human life [4–6]. For instance, the failure in repair of chronic skin wounds such as diabetic foot ulcers may lead to amputation or other life-threatening consequences [7]. Up to now, serious skin diseases remain a highly prevalent clinical problem with no satisfactory solution [8]. Therefore, it is meaning to develop

---

biomaterials with high bioactivity for regeneration of skin diseases [5].

Wound healing is a complicated process generally consisting of four successive and overlapped steps: (1) hemostasis phase; (2) inflammatory phase; (3) proliferative phase; and (4) maturation and remodeling phase [9,10]. Among them, inflammatory phase is a kind of significant procedure, where immune cells secrete pro-inflammatory cytokines to induce inflammatory cells to produce a large amount of reactive oxygen species (ROS), which are the important metabolites of oxygen, including peroxides, superoxide, the hydroxyl radical and singlet oxygen [11]. It is known that ROS are essential to protect the body against developing an infection by killing the invading pathogens [12–14]. ROS also own other positive biological functions, like collagen synthesis, angiogenesis and epithelialization [13,15,16]. ROS are involved in tissue repair by modulating cell proliferation, angiogenesis and fibrosis [17], and promote the migration and proliferation of epidermal cells [18]. ROS play an important role in signal transduction in cellular stress responses *via* activating mitogen-activated protein kinases that alleviate damage and maintain or re-establish homeostasis [17,19].

Therefore, proper ROS level may create appropriate microenvironment to activate cell survival path ways to increase cell adaptability under injured or diseased skin conditions. However, the existence of excessive ROS during a long period can induce signals towards cell apoptosis, resulting in failure in wound healing [17]. Generally, cells react to various stresses primarily through a number of specific and well conserved adaptive intracellular signaling pathways that alleviate damage and re-establish homeostasis [19]. Meanwhile, ROS overexpression is unbeneficial to angiogenesis, probably because high oxidative potential may inactivate certain enzymes with high oxidative sensitivity involved in signaling pathways (e.g., phosphotyrosine phosphatase, sulfhydryl residues) [20]. Actually, excessive ROS strain signaling networks may create an imbalanced redox homeostasis, resulting in impaired wound healing. For instance, diabetes, aging, immunodeficiency, and malnutrition are typical samples for delayed wound healing caused by overexpressed ROS [21]. Under these pathological conditions, redox imbalance occurs, which can cause an elevated oxidative injury to increase the difficulty in skin repair [22]. Therefore,

it is meaning to properly adjust the imbalanced redox homeostasis for creation of an appropriate microenvironment for skin regeneration. Naturally, redox homeostasis can be mediated by highly specialized enzymes like catalase, thioredoxins, superoxide dismutase and glutathione peroxidase as well as by naturally occurring antioxidants [23]. Disulfide-containing molecules (e.g., oxidized glutathione) can be reduced to glutathione by cytosolic glutathione reductase for adjustment of intracellular redox homeostasis [24]. Furthermore, recent report indicated that disulfide bonds are cleavable under both reducing environment and oxidizing environment [25].

These enlighten us to design a kind of wound healing materials which can act as disulfide bond reservoir for mediation of redox potential in order to promote wound healing process. Herein, we firstly developed a type of redox-sensitive nanogels by crosslinking *N*-isopropylacrylamide and acrylic acid with *N,N'*-bis(acryloyl)cystamine as biodegradable crosslinker in the presence of sodium dodecyl sulfate as surfactant. The redox nanogels were then *in situ* doped into biodegradable nanofibrous membrane of poly(L-lactic acid) (PLLA, a kind of biodegradable polymer approved by the Food and Drug Administration (FDA) [26]) *via* an airbrushing technology (a simple and effective nanofiber-spinning technique as compared to electro spinning method) [27–31]. The results indicated that nanogel introduction not only improved the mechanical strength of the native PLLA membranes, but also accelerated wound healing process (see Scheme 1).

2. Materials and methods

2.1. Materials

L-lactide was purchased from Jinan Daigang Biomaterial Co., Ltd (Jinan, China). 2′,7′-Dichlorofluorescin diacetate (DCFH-DA), hydrogen peroxide (H$_2$O$_2$), stannous octoate, 3-(4,5-dimethyl-2-thiazolyl)-2,5-diphenyl-2-*H*-tetrazolium bromide (MTT), and 4,6-diamidino-2-phenylindole (DAPI) were obtained from Sigma-Aldrich (MO, USA). N-isopropylacrylamide (NIPAM) was bought from Shanghai Xianding Biological Technology Co., Ltd (Shanghai, China). Acrylic acid (AA) was
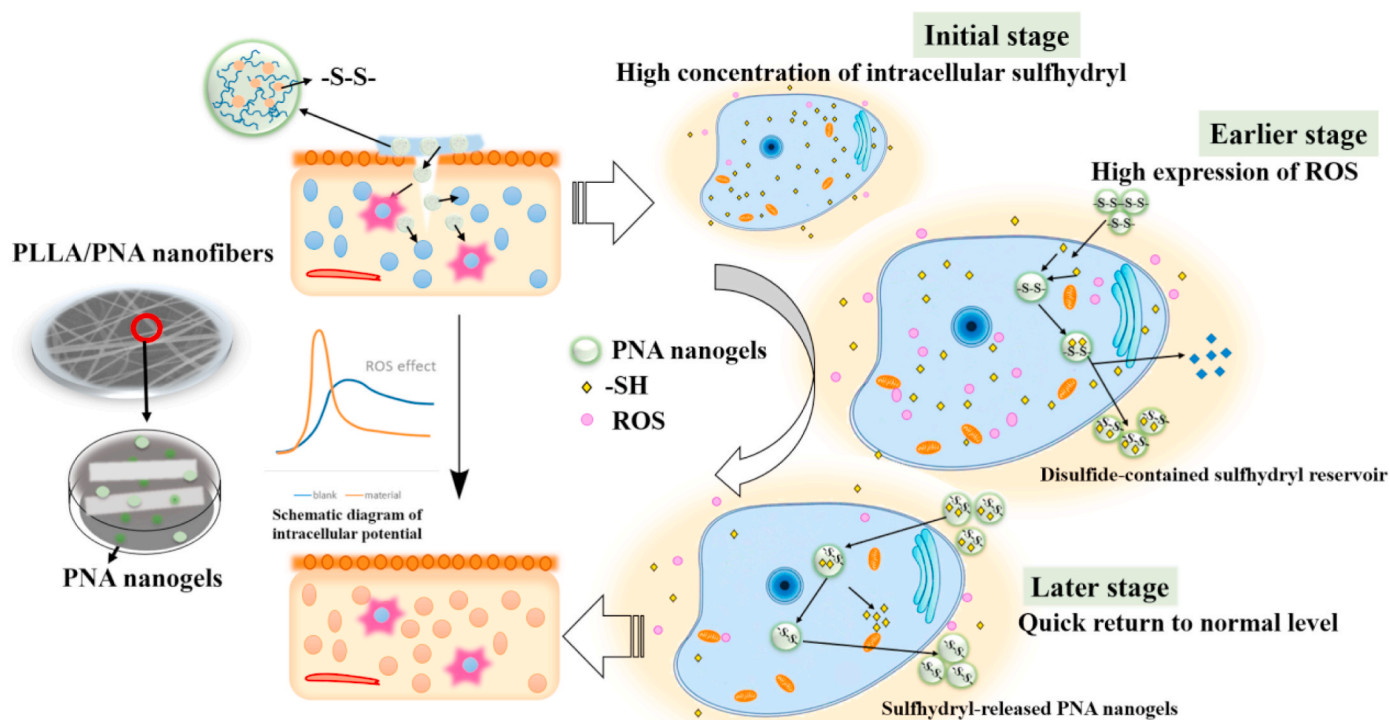
Scheme 1. The schematic diagram on fabrication of redox-sensitive nanofibrous polylactide membrane and its ROS-balance capacity for promotion of wound healing process.

bought from Shanghai Aladdin Biochemical Technology Co., Ltd (Shanghai, China). *N,N′*-bis (acryl) cysteamine (BAC) was purchased from Shanghai Titan Technology Co., Ltd (Shanghai, China). Potassium persulfate (KPS) and glutathione (GSH) were purchased from Nanjing Jiancheng Bioengineering Institute (Nanjing, China). The mouse fibroblast cell line (L929) was obtained from the Cell Bank of Chinese Academy of Sciences (Shanghai, China). C57BL/6 mice (10–12 weeks) were purchased from Shanghai Jeste Experimental Animal Co., Ltd (Shanghai, China). All other reagents were of analytical grade and used without further purification.

2.2. Preparation of redox-sensitive nanofibrous membranes

2.2.1. Synthesis of PLLA and PNA nanogels

PLLA was synthesized *via* ring-opening polymerization of ʟ-lactide at 140 °C for 6 h with Sn(Oct)$_2$ as catalyst. The coarse product was purified using a dissolving and precipitation method with ethanol and methylene chloride, followed by vacuum-dry to offer pure PLLA product. PNA nanogels were synthesized using a free radical polymerization emulsion technique. The ratio of NIPAM to AA was fixed at 14.4:1.0 and dissolved in the ultra-pure water at 70 °C under magnetic stirring for 1 h. Then initiator potassium persulfate (KPS) was added and reacted for 7 h under argon atmosphere, followed by dialysis purification for 3 d and lyophilization to obtain PNA nanogels.

2.2.2. Fabrication of redox-sensitive PNA nanofibrous membranes via airbrushing

PLLA and PLLA/PNA were dissolved in a mixed solvent of methylene chloride and ethanol under magnetic stirring for 4 h. The mixture was airbrushed on a commercial airbrush (HD-130, Syou Tools, China) with a 0.5 mm-diameter nozzle at an air pressure of 0.2 MPa (the distance from receiver to nozzle was 20 cm for all experiments). All samples were vacuum-dried to afford nanofibrous membranes containing different amount of PNA nanogels, which were abbreviated as PLLA, 5% PNA, 10% PNA and 20% PNA, respectively.

2.3. Characterization of PNA-doped nanofibrous membranes

2.3.1. Nuclear magnetic resonance (NMR) spectroscopy and gel penetration chromatography (GPC) analysis

PLLA polymer was characterized on a nuclear magnetic resonance (NMR) Spectroscope (Bruker AVANCE III 600, Bruker Corporation, Switzerland) using deuterium chloroform (CD$_3$Cl) as solvent and tetramethylsilane (TMS) as an internal standard. Gel penetration chromatography (PL-GPC50, Agilent Technologies, USA) was used to analyze the molecular weight of PLLA polymer using tetrahydrofuran as mobile phase at 1 mL/min flow rate and 35 °C with monodisperse polystyrene as a standard sample.

2.3.2. Morphology of PNA nanogels and fibrous membranes

The morphology of PNA nanogels was characterized by a transmission electron microscope (TEM, Hitachi JEM-1400, Japan) with an accelerating voltage of 200 kV. Before measurement, nanogels were dispersed in ultrapure water (0.1 mg/mL). Field emission scanning electron microscope (FESEM, Hitachi S-3400, Japan) was used to observe the morphologies of the PNA nanogels and the nanofibrous membranes at an accelerating voltage of 15 kV. Before SEM characterization, nanofiber mats were sprayed with gold for 120 s. The fiber diameters and size distributions in the nanofibrous membrane were calculated from SEM images using an image analysis software (Image J).

2.3.3. Morphological characterization

In order to study the morphology of nanogels and nanofibrous membrane, the PNA nanogels were observed on a scanning electron microscope (SEM) coupled with an energy dispersive spectrometer (EDS) (Quanta200FEG, FEI Co., Hillsboro, OR). PNA nanogels were

dispersed in ultrapure water, and the solution was dropped on glass slide, airdried, followed by gold spraying before SEM analysis at an acceleration voltage of 20 kV. For membrane observation, the dried PLLA nanofibrous membrane were cut and pasted on an electron microscopy platform with conductive adhesive before SEM observation.

2.3.4. Fourier transform infrared (FTIR) characterization

Fourier transform infrared (FTIR, Nicolet 5700, Thermo, USA) spectra of PNA nanogels as well as the nanofibrous membranes of PLLA, 5% PNA, 10% PNA and 20% PNA were measured in the wavelength range from 500 to 4000 cm^{-1}.

2.3.5. Thermal analysis

Thermal properties of the samples were scanned on a differential scanning calorimeter (DSC2910, TA Instruments, USA) at a heating or cooling rate of 10 °C/min. The curves were scanned from room temperature to 220 °C, followed by keeping the temperature at 220 °C for 5 min, and then cooled down to 10 °C. After maintaining the samples at 10 °C for 5 min, the examination of final curves was finished by increasing again the temperature to 220 °C.

2.3.6. X-ray diffraction (XRD) analysis

The crystalline structure of nanofibrous membranes were measured on a X-ray polycrystalline diffractometer (Bruker D8 Advance, Germany) with scanning angel in the range of 5–50° at a scanning speed of 3°/min. Samples were cut into circle shape of the same size.

2.3.7. Mechanical property

Mechanical properties of the samples were investigated on an electromechanical universal testing machine (CMT-2503, MTS Systems, USA) at a tensile speed of 10 mm/min. Before tensile measurements, nanofibrous membranes were cut into rectangles with 50.0 mm length × 10.0 mm width × 0.1 mm thickness.

2.3.8. Water contact angle measurement

The hydrophilicity of nanofiber mats was evaluated through a contact angle meter (JC2000D2, Zhongchen Instruments, China). Time of water droplets on samples was maintained for 15 s. Images of water droplets and values of contact angle were recorded.

2.3.9. Biodegradability study

Nanofibrous membranes (6 mg) were incubated in phosphate buffer saline (PBS, pH = 7.4) at 37 °C, and samples were collected at a specific time points. After then, the samples were washed with deionized water, lyophilized and weighed. Biodegradation Ratio was calculated by weight loss according to the following equation:

$$\text{Biodegradation Ratio (\%)} = (W_0 - W_t)/W_0 \times 100 \qquad 100$$

where W_0 is the weight of the original samples used for incubation, W_t is the sample weight at the incubation time t.

2.3.10. Cell viability

Cell viability of the PNA nanogels and the nanofibrous membranes was evaluated *via* MTT assay. Briefly, L929 cells were cultured in Dulbecco's Modified Eagle Medium (DMEM) containing 10% (v/v) fetal bovine serum (FBS, Gibco) and 1% (v/v) antibiotic-antimycotic 100* solution (AA, Gibco, with penicillin, streptomycin, and amphotericin B). The medium was supplemented with 1% (v/v) ʟ-glutamine 100* solution (Gibco) and 1% (v/v) of insulin-transferrin-selenium 100* solution (ITS, Gibco). Cells were grown at 37 °C, under a humidified atmosphere with 5% CO$_2$. Afterwards, the cells were harvested at 70–80% confluence, using trypsin-EDTA solution to detach the cells from the plastic substrate.

For cytotoxicity study, L929 cells were first plated in 48-well plates at a seeding density of 5×10^3 cells per well. After 2 day incubation, the

solutions of the PNA nanogels in PBS (pH = 7.4) were added to the cell culture medium and then incubated for 48 h at 37 °C. The mass concentrations of the nanogels were 0, 5, 10, 15, 20 and 25 μg/mL. For cytotoxicity evaluation, all samples were sterilized under ^{60}Co radiation at a dose of 10 kGy. The sterilized samples were then incubated with L929 cells at a density of 5×10^4 cells per well (2 mL DMEM) containing nanofiber mats (about 0.1 mm thickness) in 12-well plate at 37 °C for 24 h and 72 h. After cell culture, 400 μL MTT solution (5 mg/mL) was added and continued to culture for 4 h. After that, cell medium was removed and replaced with 500 μL dimethyl sulfoxide to dissolve the formazan crystals at 37 °C for 15 min under a shaking incubator. The UV absorbance of the samples was measured at 492 nm on a microplate reader (SPECTRAmax 384, Molecular Devices, USA). Blank plates in the absence of samples were set as control groups. The results were expressed as relative cell proliferation (%): $OD_{sample}/OD_{control} \times 100\%$ (n = 3).

2.3.11. Cell morphology

To observe the morphology of cells after treatments with samples, 5×10^4 cells per well were cultured at 37 °C for 24 h. After incubation, cell media was removed and washed with PBS buffer (pH = 7.4) for three times, followed by fixation with 2.5% glutaraldehyde for 7 min at 25 °C. Samples were incubated with FITC-phalloidin (20 μg/mL) for cell cytoskeleton staining (45 min) at 37 °C, and washed with PBS five times. Fixed cells were finally treated with DAPI (2 μg/mL) for cell nuclei staining (10 min) at room temperature, and washed with PBS. Fluorescent images of L929 cells were observed on a confocal laser scanning microscope (CLSM, Nikon A1R, Japan).

2.3.12. The evaluation of ROS and GSH levels in vitro

The ROS and GSH levels of L929 fibroblasts were detected under H_2O_2-induced oxidative stress state. Briefly, cells were cultured in 96-well black microporous plates (5×10^3 cells/well) for 24 h. The culture medium was removed and replaced with PBS containing 10 μM 2′,7′-dichlorofluorescin diacetate (DCFH-DA), and then the cells were stored in an incubator (5% CO_2, 37 °C) for 45 min. After then, PNA (10 μg/mL) was added to the cells for 6 h and 60 μM H_2O_2 was added subsequently. Finally, the ROS level was measured by the fluorescence microplate reader (SpectraMax M3, Molecular Devices, USA) at 500 nm excitation wavelength and 525 nm emission wavelength, and the GSH level was detected spectrophotometer (TU-1901, Pgeneral, China) at the 420 nm wavelength during different periods.

2.3.13. Skin defect models in healthy mice and diabetic mice

The wound skin defect model in healthy mice was established as follows. The procedures of animal experiment were approved by Management Committee of Laboratory Animal (Shanghai, China). Briefly, forty-five C57BL/6 mice were randomly divided into 5 groups (9 mice per group): (i) control; (ii) PLLA; (iii)5% PNA; (iv)10% PNA; (v) 20% PNA. To evaluate the ability of PLLA and PNA doped nanofibrous membranes for wound healing, two skin defects with a diameter of 5 mm were created on the back of each mouse. All membranes implanted possess a diameter of 5 mm. The untreated mice was used as control. To observe the wound-healing process, wounds were photographed at day 0, 7, 14 and 19 days.

The serious skin defects model in diabetic mice was established as follows. All animal protocols were approved by the Animal Care and Use Committee of Mudanjiang Medical University (Mudanjiang, China). C57BL/6 mice were injected with streptozotocin (STZ) (100 mg/kg, i.p.) for 2 d after overnight fast to induce the type 1 diabetes model. Blood glucose levels were measured and repeated 2 weeks later. The mice with a blood glucose level of above 16.7 mM were deemed to be diabetic. Ten diabetic mice were randomly divided into 2 groups (5 mice per group): (i) PLLA; (ii) 20% PNA. Two skin defects with a diameter of 5 mm were created on the back of each mouse. All membranes implanted possess a diameter of 5 mm. After 7 d, the healing process of the diabetic wound

was evaluated by the histological evaluation with hematoxylin-eosin (H&E) staining and Masson's trichrome staining.

2.3.14. Hematoxylin-eosin (H&E) and Masson's trichrome staining

Wound skin tissues were taken from the sacrificed mice and underwent hematoxylin-eosin (HE) and Masson staining analysis. Briefly, the wound skins of killed mice were taken out, followed by fixation with 4% paraformaldehyde solution. The removal tissues were dehydrated with ethanol solution at different concentrations and the mixture of ethanol and xylene. Tissues were embedded into paraffin and 4.5 μm thick sections were made using a tissue sectioner (Leica RM2265, Germany). After HE and Masson staining, the morphologies of skin tissues were observed on an inverted microscope (Leica DMi8, Germany).

2.3.15. The evaluation of ROS levels in vivo

ROS-sensitive DCFH-DA was used to detect the ROS produced in vivo. Briefly, 6 diabetic mice were randomly divided into two groups (3 mice per group): (i) untreated; (ii) 20% PNA. Firstly, a solution of 1 mg/mL^{-1} DCFH-DA was smeared on the back skin of diabetic mice, and 20% PNA nanofibrous membrane was then applied to the wound. Fluorescence images were then taken at set interval time points (50, 90 and 130 min after DCFH-DA was smeared), using the Night Owl In Vivo Imaging System (LB983 NC100, Berthold, Germany). A 520 nm filter was used to measure the fluorescence signal emitted by the fluorescein produced from the oxidation of DCFH-DA.

2.4. Statistical analysis

Data in this study were analyzed using SPSS 13.0 software (SPSS, Inc., IL, USA). Student's unpaired *t*-test and One-way Analysis of Variance with Dunnett's or Newman Keul's post-tests were used. Differences with *P* values of less than 0.05 indicated significance. *$P < 0.05$; **$P < 0.01$; ***$P < 0.001$; n.s. represents not significant ($P > 0.05$).

3. Results and discussion

3.1. Structure and molecular weight analysis of PLLA

The chemical structure of PLLA polymer was analyzed by NMR (Fig. 1a). PLLA offered a chemical shift at $\delta = 1.56$ ppm corresponding to methyl group on the polymer chain, and a chemical shift at $\delta = 5.16$ ppm related to the methylene group on the polymer framework, indicating a successful synthesis of PLLA polymer [32]. Gel penetration chromatography (GPC) is a common method for molecular weight measurement of polymers. By GPC analysis, PLLA had a weight molecular weight of 524 kDa with a relative low polydispersity index (PDI) of 1.46.

3.2. Preparation and characterization of redox-sensitive PNA nanogels and PNA -doped nanofibrous membranes

PNA nanogels were synthesized *via* radical polymerization nanoprecipitation approach [33]. N-isopropylacrylamide (NIPAM) and acrylic acid (AA) were selected as free radical polymerization monomers and *N,N′*-bis(acryloyl)cystamine (BAC) as a crosslinker. The morphology of PNA nanogels was observed by transmission electron microscopy (TEM). As shown in Fig. 1b, PNA nanogels had a nanosize of ~100 nm with a relatively narrow size distribution. After 1 h treatment with 5 mM GSH, the PNA nanogels became blurred, suggesting their cleavability under reducible microenvironments probably due to the adsorption of thiol groups which broke down the disulfide crosslinks in the nanogels. Airbrushing technique, as a simple and efficient nanofiber spinning technique, was selected for preparation of biodegradable nanofibrous membranes. The morphology and structure of airbrushed membranes were characterized by scanning electron microscopy (SEM). As shown in Fig. 2, all the membranes assumed a nanofibrous structure with fiber diameters of 100–500 nm, suggesting nanogel-dopant did not exert an
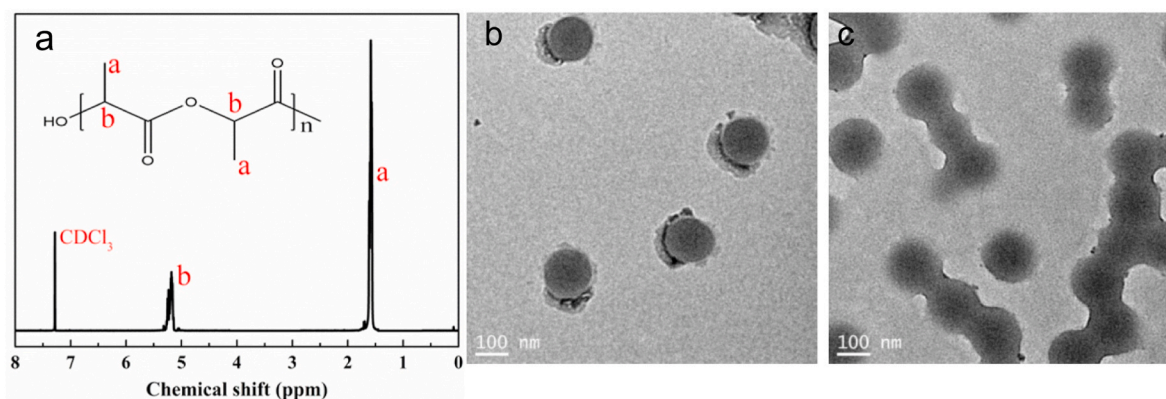
Fig. 1. Structural characterization of PLLA and PNA nanogels. (a) NMR of PLLA; TEM micrographs of PNA nanogels before (b) and after (c) treatment with 5 mM GSH for 1 h.
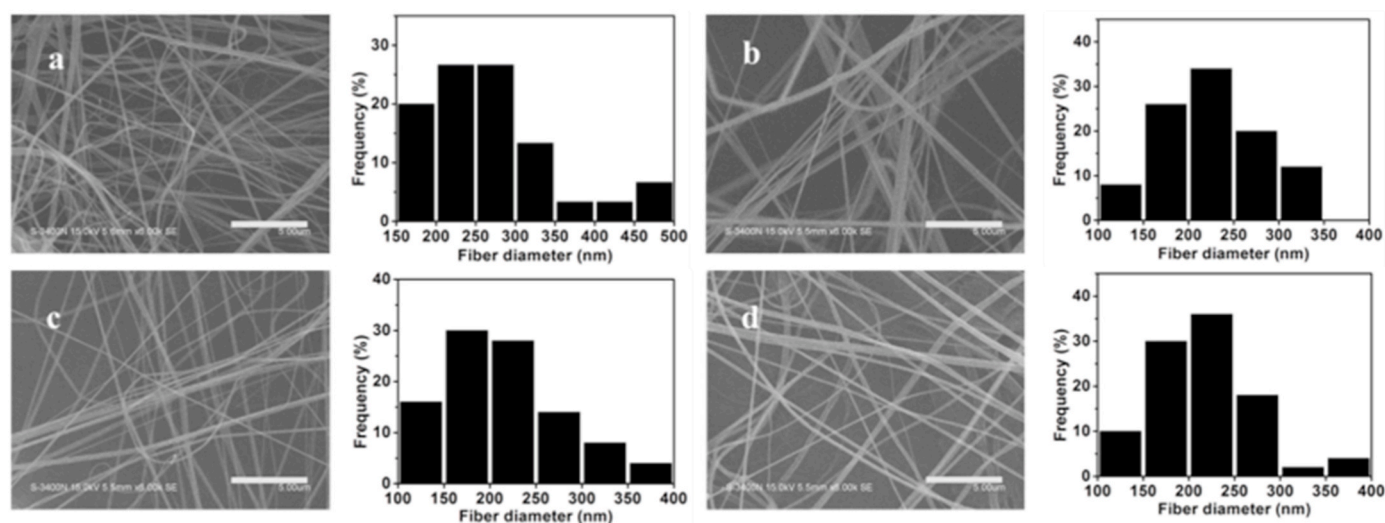

Fig. 2. SEM micrographs of the nanofibrous membranes: (a) PLLA, (b) 5% PNA, (c) 10% PNA, (d) 20% PNA. Scale bars: 5 μm.

obvious effect on nanofibrous structure.

Since PNA nanogels contains disulfide crosslinks and nitrogen elements which are absent in the PLLA, these components can be used for investigation of the distribution of PNA nanogels in the PLLA membrane. We therefore investigated the distribution of PNA nanogel in the PLLA membrane via the energy dispersive spectroscopy (EDS) technique mostly used for composition analysis of materials. The results indicated that both S and N elements were detected and relatively homogeneously distributed in the membrane, suggesting a uniform nanogel-hybridized membrane formation (Fig. S1).

Fourier transform infrared spectroscopy (FTIR) was used to check the microstructure of PNA nanogels as well as the nanofibrous membranes. As shown in Fig. 3c, PLLA membrane gave two absorption peaks at 1757 cm^{-1} and 1092 cm^{-1} corresponding to the stretching vibrations of C=O and C–O, respectively [34]. The absorption peak of C=O (amide I) stretching vibration was observed at 1645 cm^{-1} in the PNA-doped membranes (5% PNA, 10% PNA, 20% PNA), and the absorption peaks of 1539 cm^{-1} and 3301 cm^{-1} came from N–H stretching vibration bond [35]. Meanwhile, all the hybrid membranes presented the absorption peaks at 1525 cm^{-1} (N–H) and 1648 cm^{-1} (C=O) [35], again indicating that PNA nanogels have been successfully incorporated in the PLLA nanofibrous membranes through the airbrushing approach.

The mechanical properties of biomaterials play a critical role in regulating cell behaviors, such as cell migration, spreading and adhesion [36]. It is reported that "tissue cells feel and respond to the stiffness of

their substrates" in an active way [36]. For skin regeneration, it is desirable to develop a kind of regenerative membrane that are similar in stiffness to skin itself. As shown in Fig. 3a and b, all the nanofibrous membranes had a Young's modulus of 2 MPa–11 MPa, which is in the same range of skin's stiffness (5 MPa–30 MPa) [37]. The similarity in stiffness could make skin cells prefer to grow on the membrane surface for wound healing [38]. Furthermore, the variation of the PNA nanogel amount allows for adjustment of the mechanical properties in a controllable way (tensile strength from 150 kPa to 350 kPa; Modulus from 2 MPa to 11 MPa in this study) for a specific biomedical application beyond wound healing.

The surface characteristics of materials, including surface hydrophilicity and charges, have a significant impact on cell behaviors [39, 40]. In this case, the hydrophobicity of PLLA polymer greatly limits its biomedical application [32]. The hydrophilicity of PLLA and PNA-doped nanofibrous membranes was evaluated using a water contact angle test at room temperature. As was shown in Fig. 3d, the increase of PNA proportion from 0 to 20% led to the decrease of the water contact angles of the nanofibrous membrane from $(121.1 \pm 3.1)°$ to $(71.2 \pm 4.8)°$. It has been reported that biomaterial in moderate hydrophilicity with contact angle of 40°–60° is beneficial to cell proliferation in an optimal way [39]. Therefore, a suitable level of hydrophilicity could be well adjusted by varying the proportion of PNA nanogels, offering proper microenvironments for skin-related cell attachment and proliferation for wound healing. It is well known that PLLA is a kind of biodegradable polymer
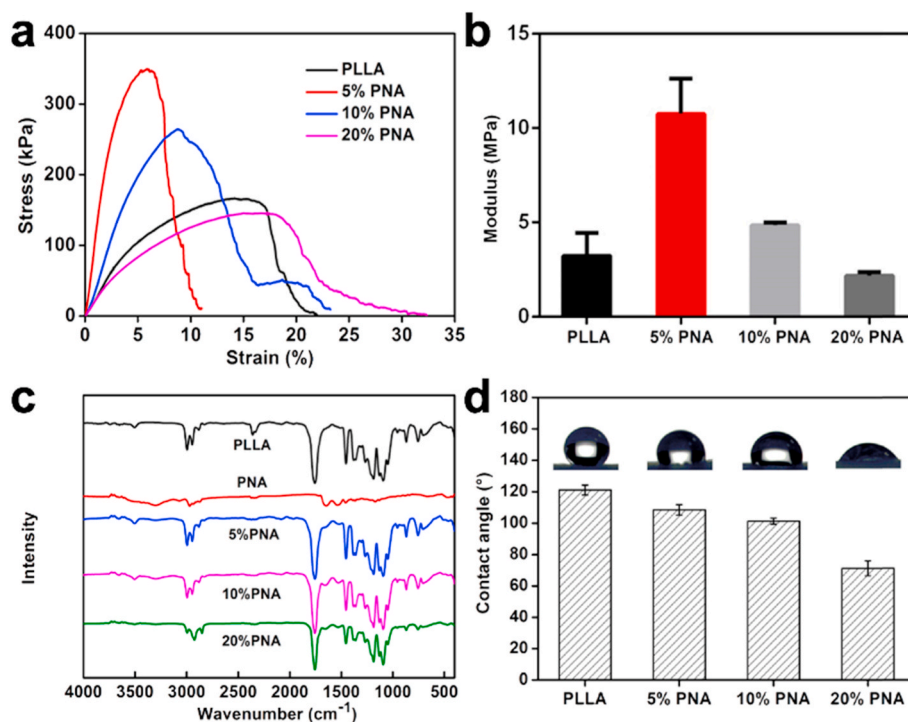
Fig. 3. Mechanical properties of PLLA and PNA-doped nanofibrous membranes: (a) tensile curves and (b) Young's modulus at different PNA doping concentrations; (c) FTIR spectra of PNA nanogels, as well as PLLA and PNA-dopped nanofibrous membranes; (d) The effect of PNA nanogel amount on the water contact angles of PNA-doped nanofibrous membranes. Data are represented as mean $\pm$ SD (n = 3).

approved by the Food and Drug Administration (FDA) [19]. The in vitro degradation rate of the membrane has been performed. As shown in Fig. S2, the incorporation of PNA nanogels accelerated the degradation speed of the membrane, probably because of the higher hydrophilicity of the PNA modified membranes which enhanced their water adsorption ability and erosion capacity [32] (Fig. 3d).

3.3. In vitro cell study

Materials should present high biocompatibility for biomedical application [41]. Cell viability of L929 cells cultured with the samples was evaluated via MTT assay. As shown in Fig. 4a, all cells treated with PNA nanogels (with concentration up to 25 mg/mL) presented $\sim$ 125% cell viability, suggesting their good biocompatibility for promotion of cell growth. The cytocompatibility of PLLA and PNA-doped nanofibrous membranes was further assessed using the MTT assay. It can be seen from Fig. 4b, after 1 d incubation, L929 cells treated with all membranes exhibited high cell viability (above 100%), which could be attributed to the good biocompatibility of PLLA and PNA nanogels [33,42]. With incubation time extension to 3 d, all the membranes greatly promoted

cell growth compared to cell dish as control, possibly because their nanofibrous structure offers high porosity and large specific surface area for cell adhesion [43]. At day 3, the PNA-doped nanofibrous membranes showed higher cell proliferation than pure PLLA nanofibrous membrane. The increase of PNA portion in the membrane resulted in a gradual increase in cell viability at day 3, probably because the improved hydrophilicity of the PNA-doped membranes with ROS balance capacity can benefit cell adhesion and proliferation in a more favorable manner [39].

Cell morphology is an important factor closely associated with cell functions (e.g., cell proliferation, differentiation and apoptosis). The lack of cell-material interactions may result in poor cell attachment and spreading to cause cell apoptosis [44,45]. In order to study the morphology of cells cultured on materials, L929 cells were treated with the nanofibrous membranes for 1 d, and the fluorescent images of L929 cells on the membranes were visualized by laser scanning confocal microscopy. As shown in Fig. 5, compared to native PLLA nanofibrous membrane, cells cultured on the PNA-doped ones presented better cell attachment and fusiform spreading shape. This again indicates that the adjustment of PNA content into PLLA membrane is useful for regulation of cell adhesion, spreading and proliferation, probably due to the high
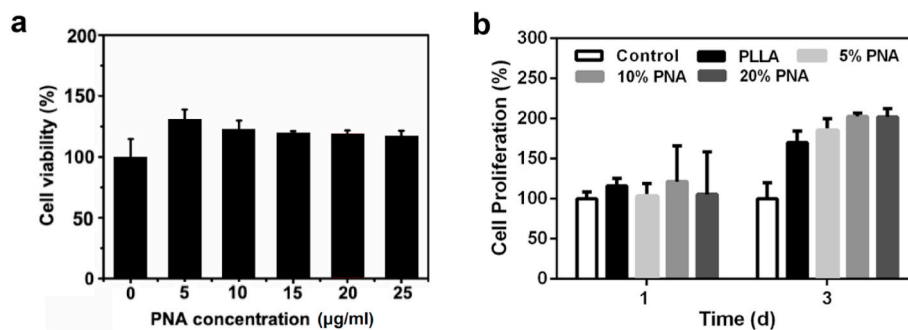

Fig. 4. The biocompatibility of PNA nanogels and membranes: (a) Cell viability of L929 cells treated with PNA nanogels for 2 d. (b) Cell proliferation of L929 cells cultured with PLLA and PNA-doped nanofibrous membranes for 1 d and 3 d. Data are represented as mean $\pm$ SD (n = 3).

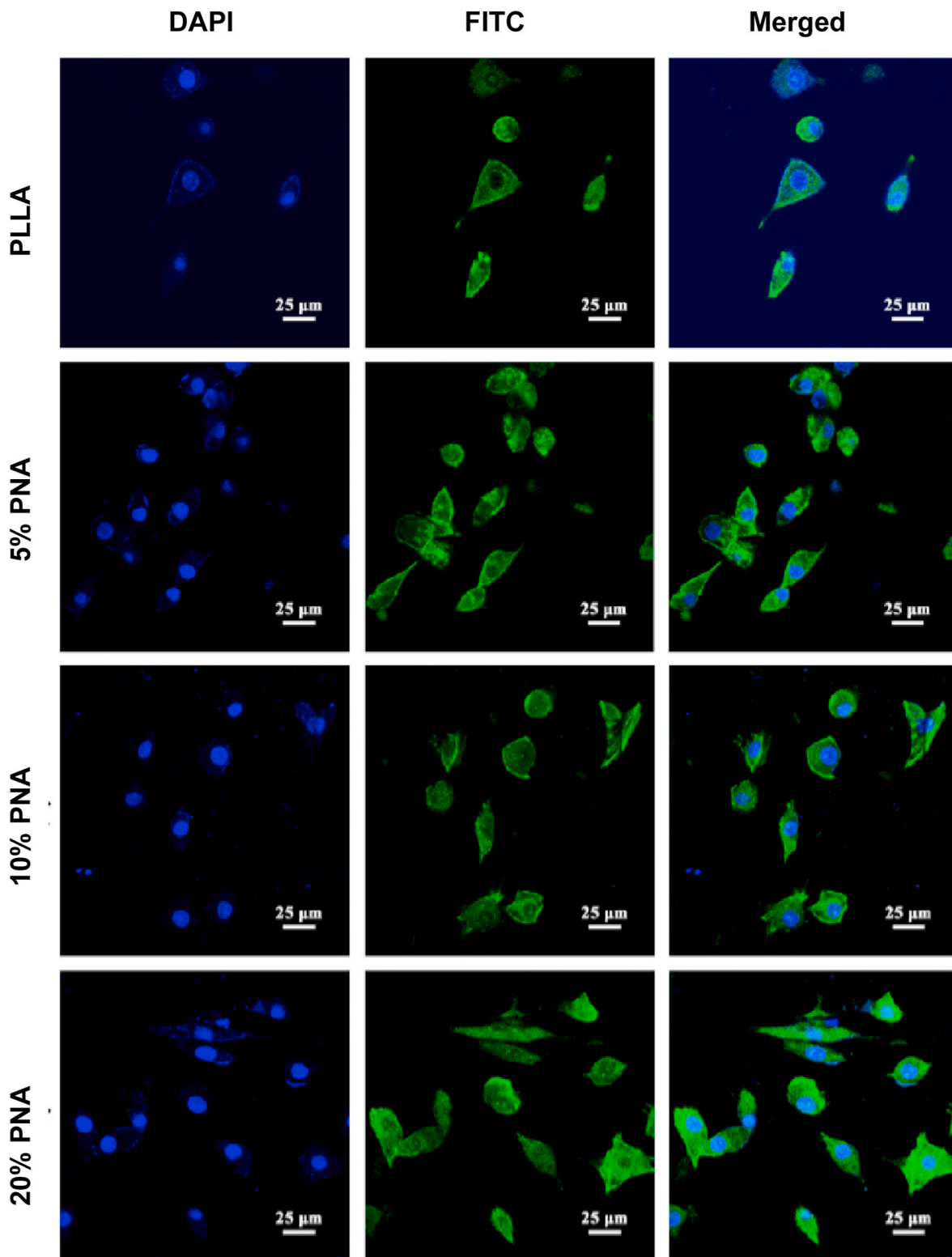| DAPI	FITC	Merged

Fig. 5. Fluorescent images of L929 cells on PLLA and PNA-doped nanofibrous membranes after 1 d incubation. Scale bars:25 μm.

biocompatibility of redox-sensitive PNA nanogels as well as their improvement in the membrane's hydrophilicity (Figs. 3d and 4a).

3.4. In vivo wound healing assessment

To evaluate the capacity of PLLA and PNA-doped nanofibrous membranes for wound healing, two skin defects of 5 mm diameter were created in each mouse and were filled with five kinds of nanofibrous constructs (blank without materials as control, PLLA and 5% PNA, 10% PNA, and 20% PNA). Fig. 6a showed that digital pictures of skin wounds of the mice treated at different treating period. The photographic evaluation indicated that mice covered with PNA-modified membranes showed an accelerated healing process, especially at day 14 and day 19. The improved wound healing may come from the high biocompatibility
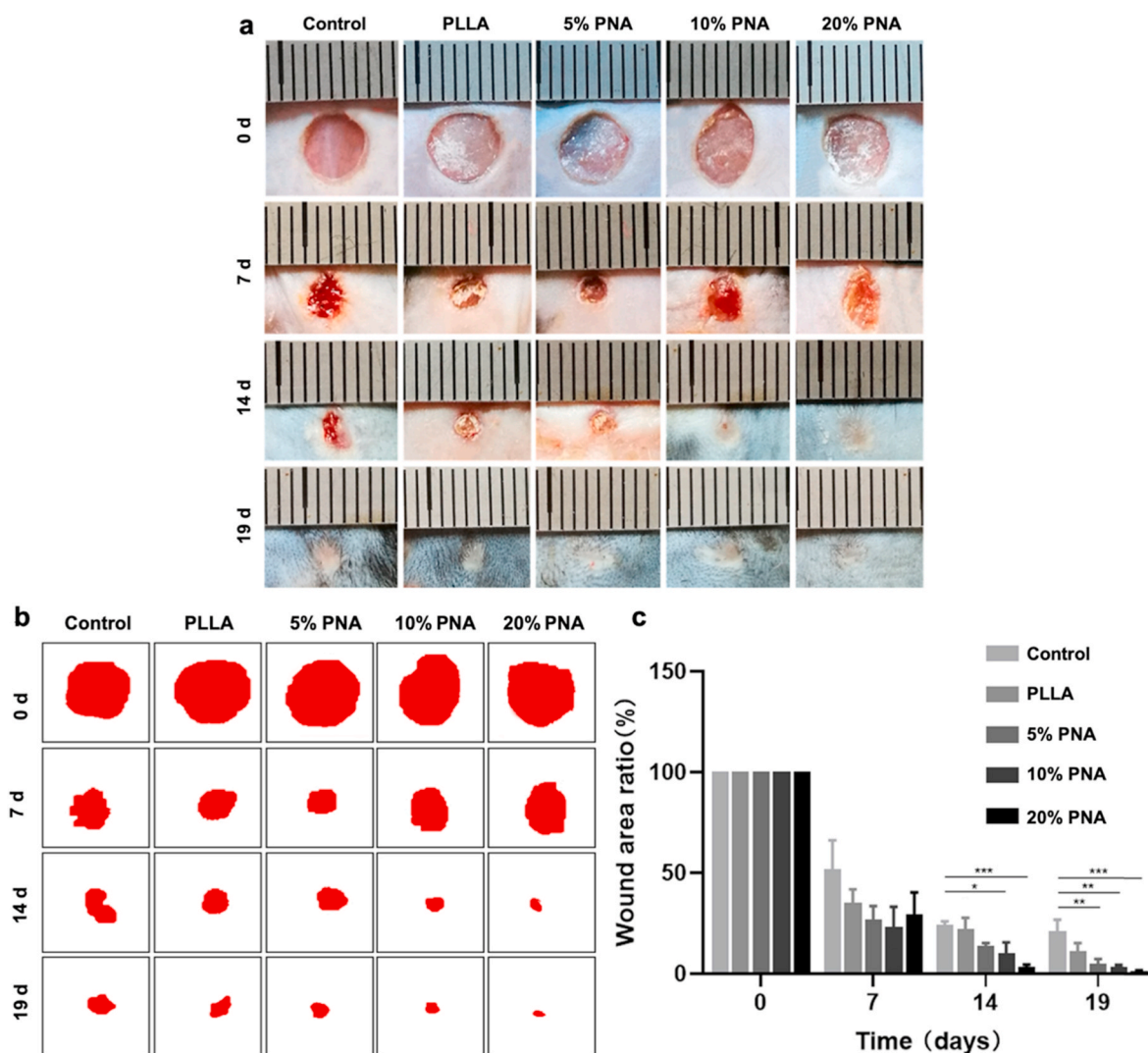
Fig. 6. Healing process evaluation of skin wound after treatment with different samples. (a) representative digital photos of wound area of mice treated with control, PLLA, 5% PNA, 10% PNA or 20% PNA; (b) the simulated unhealed skin areas of the mice, and (c) the unhealed ratios of the mice after treatment. Data are represented as mean ± SD (n = 6). *$P < 0.05$, **$P < 0.01$, ***$P < 0.001$.

of disulfide-containing PNA nanogels in the membranes, which can absorb –SH groups to increase ROS concentration in the early time. The reduced –SH could be again transformed into disulfide bonds by absorbing the excessive ROS to restore to the normal ROS state. Therefore, the ROS-balance capacity can accelerate the inflammatory response at early stage [45], while reducing the inflammatory response at late stage [46] to create favorable conditions for wound healing. Also, the PNA-induced increase in membrane's hydrophilicity can improve skin regeneration by promoting cell migration, attachment and proliferation of skin related cells (e.g., fibroblasts) (Figs. 3d and 5).

Fig. 7a and Fig. 7b indicate the hematoxylin-eosin (H&E) staining of the experimental groups (PLLA membrane and 20% PNA membrane) and control group. At 7 d, abundant inflammatory cells were infiltrated into the upper layers of dermis in the wound site in the control group, possibly because severe inflammation occurred at the wound site due to the lack of external protection [9,10]. Compared with the control group, mice treated with PLLA membrane displayed a significant decrease in inflammatory cells at the wound site. 20% PNA group further decreased the number of inflammatory cells probably because the redox-sensitive PNA nanogels balanced the excessive ROS state to normal level to effectively reduce high intense inflammatory response at the late wound healing stage. Meanwhile, epidermis and mature granulation tissue were formed for 20% PNA group compared to PLLA group. After 7

d treatment, 20% PNA nanofibrous membrane was combined closely with skin tissue. As comparison, clear separation still existed between the PLLA membrane and skin tissue. This is because the PLLA's hydrophobicity prevented cell attachment, migration and growth, while 20% PNA group with more hydrophilicity and ROS-balance capacity could increase skin-related cell migration and proliferation due to its better affinity with skin tissues.

After 14 d, new epidermis was formed in the wound surface covered with PLLA and PNA-doped membrane, while no epidermis was formed in the control group (Fig. 7b). Compared to the PLLA group, wound skin treated with 20% PNA membrane almost completed re-epithelialization to form an increased thickness in the newly regenerated epidermis. Also, mice treated with 20% PNA membrane produced abundant collagen fibers with more ordered arrangement, compared to the irregularly disordered collagen fibers for the PLLA group. At the period of 19 d, compared to the control group and PLLA group, dermal and epidermal structures were more complete in the PNA group, allowing for formation of new skin appendages (e.g., sweat gland) and blood vessel.

The above results demonstrate that PLLA and PNA-doped nanofibrous membranes possessed the wound healing ability in skin wound. Therefore, we next examined the wound healing ability of them using a full-thickness diabetic wound model. Fig. S3 shows that H&E and Masson's trichrome staining of wound samples were evaluated the
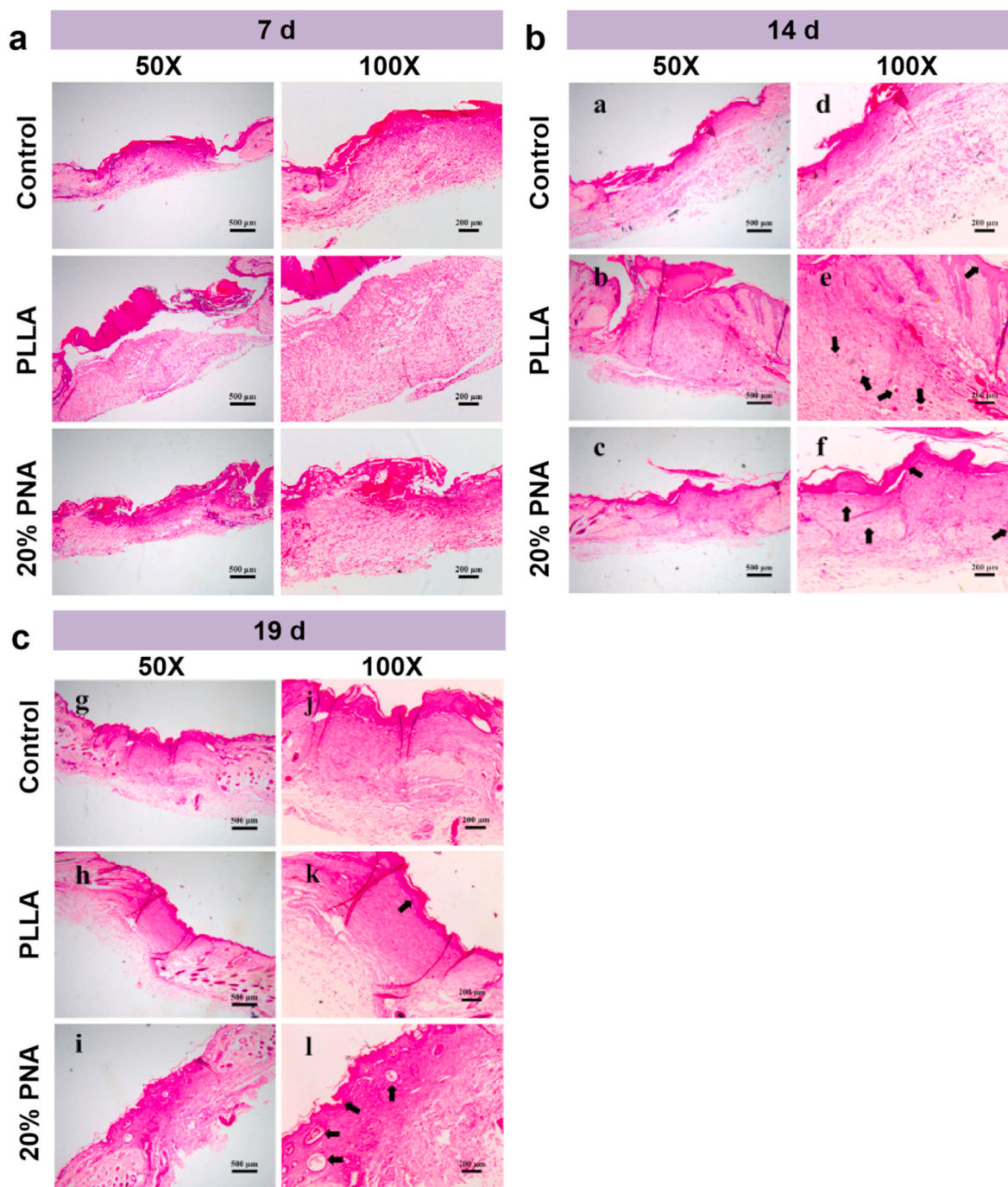
Fig. 7. The histological evaluation of skin wound after treatment with samples (Control, PLLA and 20% PNA). Hematoxylin-eosin (H&E) staining sections of skin wound for (a) 7 d, (b) 14 d and (c) 19 d.

histological status at 7 d. The degree of re-epithelization in 20% PNA-doped PLLA treated skin wounds was also significantly greater than that in PLLA group. Moreover, thick abundant granulation tissue can be clearly seen in the 20% PNA group, while wounds in the PLLA group showed a very small amount of newly formed tissue. The 20% PNA group showed good healing status, which is better than the PLLA group. This again indicated that 20% PNA membrane can promote wound healing process, probably because the ROS-mediated capacity of the PNA-doped membrane can promote the migration and growth of skin related cells (endothelial cells, fibroblasts, keratinocyte) for acceleration of blood vessel reformation and skin regeneration [47].

To check the ROS-mediated capacity on skin regeneration, the in vivo ROS-regulation effect of PNA nanogels on oxidative stress state was

evaluated on a diabetic mice model. The in vivo ROS levels of the wound skin in the absence (Control) and presence of the 20% PNA membrane were investigated by using the ROS detection kit and living animal imaging system (Fig. 8a). The results indicated that ROS fluorescent intensity in the wound skin continuously increased from 261 ± 6 a.u. to 422 ± 10 a.u. at 50 min and 130 min, while the 20% PNA-treatment resulted in a higher ROS fluorescent intensity of 358 ± 6 a.u. at 50 min, followed by a rapid rebalance to a lower level of 233 ± 25 a.u. (Fig. 8b).

To further investigate the regulatory mechanism of PNA nanogels, we examined the intracellular levels of both ROS and glutathione (GSH). The intracellular ROS level was estimated using DCFH-DA as a fluorescent probe. Similar to the in vivo result, the cellular ROS level in
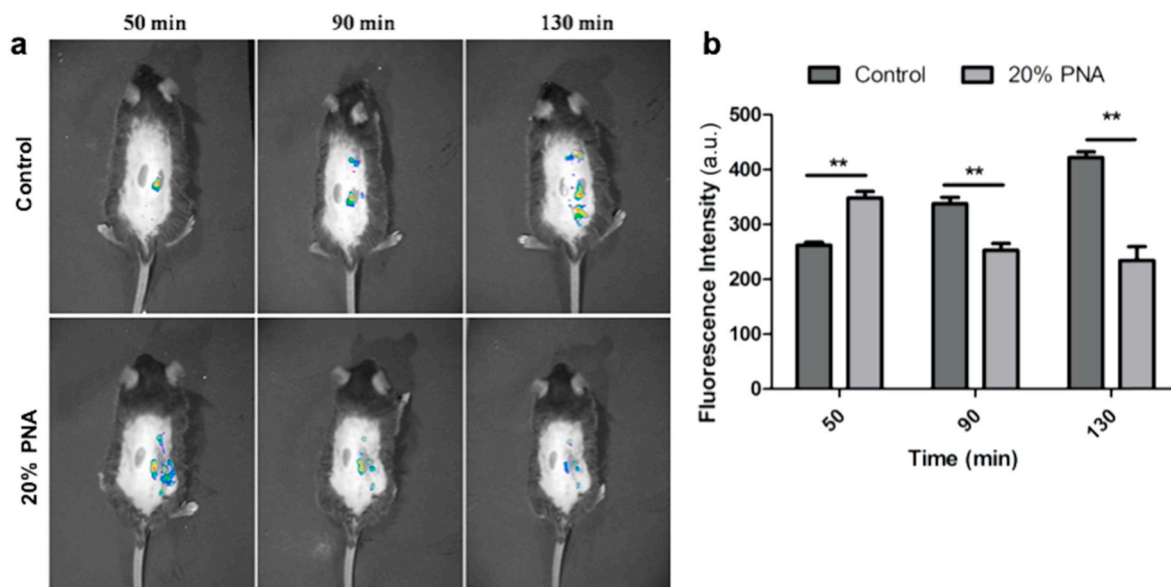
Fig. 8. Optical in vivo imaging showing intensity and durability of ROS fluorescence signals: (a) ROS production was monitored by DCFH-DA. (b) The integrated relative ROS fluorescent intensity was quantified at different time points. Data are represented as mean $\pm$ SD (n = 3). *$P < 0.05$, **$P < 0.01$, ***$P < 0.001$.

fibroblasts also gradually increased under oxidative stress mimicking condition (induced by H_2O_2), while at the same condition the PNA nanogels-treated sample displayed a higher ROS level at the beginning, and maintained a relatively lower level at later periods (Fig. 9a). Meanwhile, the GSH levels regulated by different samples were detected by the GSH detection kit. As shown in Fig. 9b, under oxidative stress mimicking condition (induced by H_2O_2), the PNA nanogels could adjust the GSH level to a normal level to reduce the long-term oxidative stress damage [19]. These results, together with the PNA nanogel morphology change in the presence of 5 mM GSH (Fig. 1b and c), again indicated the good redox-adaptability of the PNA nanogels. The ROS adaptability may enable to provide appropriate microenvironmental feature to adjust the ROS level in the wound skin for mediation of redox potential to achieve higher wound healing efficacy (increased expression of immune cells-secreted pro-inflammatory cytokines at the initial stage, followed by re-adjustment to a low ROS level to alleviate damage and re-establish homeostasis) [19]. Taken together, the above results indicate the PNA nanofibrous membrane owns a ROS-balance capacity which is beneficial to accelerate the wound healing efficacy.

4. Conclusions

In the work, redox-sensitive poly(N-isopropylacrylamide-acrylic acid) (PNA) nanogels were synthesized *via* free radical nanoprecipitation polymerization technique, which were *in situ* doped into polylactide matrix to obtain bioabsorbable membrane with redox-sensitivity *via* airbrushing approach. The PNA introduction can improve the hydrophilicity of the nanofibrous membrane, which together with its redox-sensitive ROS-balance capacity promoted cell adhesion and proliferation in a better way compared to the hydrophobic polylactide membrane. The PNA-doped nanofibrous membranes with multi-functions greatly accelerate skin regeneration during the wound healing process.

CRediT authorship contribution statement

Shihao Zhang: Methodology, Investigation, Validation, Formal analysis, Data curation, Formal analysis, Visualization. **Yamin Li:** Methodology, Investigation, Validation, Formal analysis, Data curation, Formal analysis, Visualization. **Xiaofeng Qiu:** Methodology, Investigation, Validation, Formal analysis, Data curation, Formal analysis, Visualization. **Anqi Jiao:** Investigation, Data curation, Formal analysis. **Wei Luo:** Investigation, Validation, Formal analysis, Software. **Xiajie Lin:** Data curation, Methodology. **Xiaohui Zhang:** Investigation, Methodology. **Zeren Zhang:** Investigation, Methodology, Data curation. **Jiachan Hong:** Investigation. **Peihao Cai:** Formal analysis. **Yuhong Zhang:**
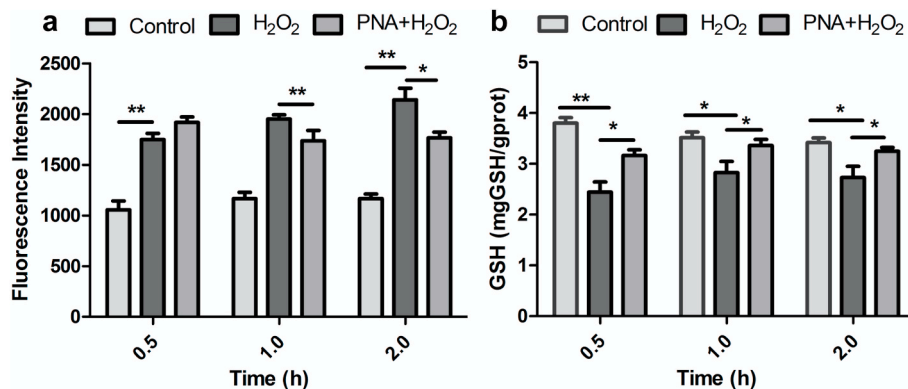
Fig. 9. The redox-balance activity of PNA nanogels: (a) Quantitative analysis of the ROS level by fluorescence measurement. (b) GSH content analysis by spectrophotometer. Data are represented as mean $\pm$ SD (n = 5). *$P < 0.05$, **$P < 0.01$, ***$P < 0.001$.

Investigation, Methodology. **Yan Wu:** Investigation, Formal analysis, Writing – review & editing. **Jie Gao:** Investigation, Formal analysis, Writing – review & editing. **Changsheng Liu:** Supervision, Resources, Funding acquisition, Project administration. **Yulin Li:** Conceptualization, Methodology, Investigation, Validation, Formal analysis, Writing – original draftWriting - original draft, Funding acquisition, Supervision, Writing – review & editing.

Declaration of competing interest

Acknowledgements

Appendix A. Supplementary data

Supplementary data to this article can be found online at https://doi.org/10.1016/j.bioactmat.2021.03.009.

References

[1] A.L. Clement, T.J. Moutinho Jr., G.D. Pins, Micropatterned dermal-epidermal regeneration matrices create functional niches that enhance epidermal morphogenesis, Acta Biomater. 9 (2013) 9474–9484.

[2] M. Santoro, S.R. Shah, J.L. Walker, A.G. Mikos, Poly(lactic acid) nanofibrous scaffolds for tissue engineering, Adv. Drug Deliv. Rev. 107 (2016) 206–212.

[3] V.J. Reddy, S. Radhakrishnan, R. Ravichandran, S. Mukherjee, R. Balamurugan, S. Sundarrajan, S. Ramakrishna, Nanofibrous structured biomimetic strategies for skin tissue regeneration, Wound Repair Regen. 21 (2013) 1–16.

[4] Y. Wang, J. Beekman, J. Hew, S. Jackson, A.C. Issler-Fisher, R. Parungao, S. S. Lajevardi, Z. Li, P.K.M. Maitz, Burn injury: challenges and advances in burn wound healing, infection, pain and scarring, Adv. Drug Deliv. Rev. 123 (2018) 3–17.

[5] L. Chen, L. Cheng, Z. Wang, J. Zhang, X. Mao, Z. Liu, Y. Zhang, W. Cui, X. Sun, Conditioned medium-electrospun fiber biomaterials for skin regeneration, Bioact. Mater. 6 (2021) 361–374.

[6] H. Chen, J. Cheng, L. Ran, K. Yu, B. Lu, G. Lan, F. Dai, F. Lu, An injectable self-healing hydrogel with adhesive and antibacterial properties effectively promotes wound healing, Carbohydr. Polym. 201 (2018) 522–531.

[7] K.H. Park, J.B. Kwon, J.H. Park, J.C. Shin, S.H. Han, J.W. Lee, Collagen dressing in the treatment of diabetic foot ulcer: a prospective, randomized, placebo-controlled, single-center study, Diabetes Res. Clin. Pract. 156 (2019) 107861.

[8] N. Fereydouni, M. Darroudi, J. Movaffagh, A. Shahroodi, A.E. Butler, S. Ganjali, A. Sahebkar, Curcumin nanofibers for the purpose of wound healing, J. Cell. Physiol. 234 (2019) 5537–5554.

[9] K.A. Rieger, N.P. Birch, J.D. Schiffman, Designing electrospun nanofiber mats to promote wound healing - a review, J. Mater. Chem. B 1 (2013) 4531–4541.

[10] W. Liu, M. Wang, W. Cheng, W. Niu, M. Chen, M. Luo, C. Xie, T. Leng, L. Zhang, B. Lei, Bioactive antiinflammatory antibacterial hemostatic citrate-based dressing with macrophage polarization regulation for accelerating wound healing and hair follicle neogenesis, Bioact. Mater. 6 (2021) 721–728.

[11] D.K. Ji, Y. Zhang, Y. Zang, J. Li, G.R. Chen, X.P. He, H. Tian, Targeted intracellular production of reactive oxygen species by a 2D molybdenum disulfide glycosheet, Adv. Mater. 28 (2016) 9356–9363.

[12] Y.H. Kim, S.H. Lee, Mitochondrial reactive oxygen species regulate fungal protease-induced inflammatory responses, Toxicology 378 (2017) 86–94.

[13] M. Mittal, M.R. Siddiqui, K. Tran, S.P. Reddy, A.B. Malik, Reactive oxygen species in inflammation and tissue injury, Antioxidants Redox Signal. 20 (2014) 1126–1167.

[14] Z. Chen, J. Duan, Y. Diao, Y. Chen, X. Liang, H. Li, Y. Miao, Q. Gao, L. Gui, X. Wang, J. Yang, Y. Li, ROS-responsive capsules engineered from EGCG-Zinc

[15] R.E. McDowell, C.D. Amsler, D.A. Dickinson, J.B. McClintock, B.J. Baker, Reactive oxygen species and the Antarctic macroalgal wound response, J. Phycol. 50 (2014) 71–80.

networks improve therapeutic angiogenesis in mouse limb ischemia, Bioact. Mater. 6 (2021) 1–11.

[16] S. Schreml, R.M. Szeimies, L. Prantl, S. Karrer, M. Landthaler, P. Babilas, Oxygen in acute and chronic wound healing, Br. J. Dermatol. 163 (2010) 257–268.

[17] H.A. Rather, R. Thakore, R. Singh, D. Jhala, S. Singh, R. Vasita, Antioxidative study of Cerium Oxide nanoparticle functionalised PCL-Gelatin electrospun fibers for wound healing application, Bioact. Mater. 3 (2018) 201–211.

[18] P. Niethammer, C. Grabher, A.T. Look, T.J. Mitchison, A tissue-scale gradient of hydrogen peroxide mediates rapid wound detection in zebrafish, Nature 459 (2009) 996.

[19] F. Jiang, Y. Zhang, G.J. Dusting, NADPH oxidase-mediated redox signaling: roles in cellular stress response, stress tolerance, and tissue repair, Pharmacol. Rev. 63 (2011) 218–242.

[20] S.H. Cho, C.H. Lee, Y. Ahn, H. Kim, H. Kim, C.Y. Ahn, K.S. Yang, S.R. Lee, Redox regulation of PTEN and protein tyrosine phosphatases in H2O2-mediated cell signaling, FEBS Lett. 560 (2004) 7–13.

[21] S. Ellis, E.J. Lin, D. Tartar, Immunology of wound healing, Curr. Derm. Rep. 7 (2018) 350–358.

[22] A.M. Rasik, A. Shukla, Antioxidant status in delayed healing type of wounds, Int. J. Exp. Pathol. 81 (2000) 257–263.

[23] E. Novo, M. Parola, The role of redox mechanisms in hepatic chronic wound healing and fibrogenesis, Fibrogenesis Tissue Repair 5 (2012) S4. -S4.

[24] Y. Elbaz-Alon, B. Morgan, A. Clancy, T.N.E. Amoako, E. Zalckvar, T.P. Dick, B. Schwappach, M. Schuldiner, The yeast oligopeptide transporter Opt2 is localized to peroxisomes and affects glutathione redox homeostasis, FEMS Yeast Res. 14 (2014) 1055–1067.

[25] C. He, Q. Yang, L. Tan, B. Liu, Z. Zhu, B. Gong, Y.-M. Shen, Z. Shao, Design and synthesis of redox and oxidative dual responsive block copolymer micelles for intracellular drug delivery, Eur. Polym. J. 85 (2016) 38–52.

[26] E. Lizundia, E. Meaurio, J.M. Laza, J.L. Vilas, L.M. Leon Isidro, Study of the chain microstructure effects on the resulting thermal properties of poly(L-lactide)/poly (N-isopropylacrylamide) biomedical materials, Mater. Sci. Eng. C 50 (2015) 97–106.

[27] C.T. Kenry, Lim, Nanofiber technology: current status and emerging developments, Prog. Polym. Sci. 70 (2017) 1–17.

[28] J.L. Daristotle, A.M. Behrens, A.D. Sandler, P. Kofinas, A review of the fundamental principles and applications of solution blow spinning, ACS Appl. Mater. Interfaces 8 (2016) 34951–34963.

[29] S. Srinivasan, S.S. Chhatre, J.M. Mabry, R.E. Cohen, G.H. McKinley, Solution spraying of poly(methyl methacrylate) blends to fabricate microtextured, superoleophobic surfaces, Polymer 52 (2011) 3209–3218.

[30] A.M. Behrens, B.J. Casey, M.J. Sikorski, K.L. Wu, W. Tutak, A.D. Sandler, P. Kofinas, In situ deposition of PLGA nanofibers via solution blow spinning, ACS Macro Lett. 3 (2014) 249.

[31] W. Tutak, S. Sarkar, S. Lin-Gibson, T.M. Farooque, G. Jyotsnendu, D. Wang, J. Kohn, D. Bolikal, C.G. Simon, The support of bone marrow stromal cell differentiation by airbrushed nanofiber scaffolds, Biomaterials 34 (2013) 2389–2398.

[32] Y. Yang, X. Qiu, Y. Sun, Y. Wang, J. Wang, Y. Li, C. Liu, Development of bioabsorbable polylactide membrane with controllable hydrophilicity for adjustment of cell behaviours, Roy. Soc. Open. Sci. 5 (2018) 170868.

[33] Y. Zhan, M. Goncalves, P. Yi, D. Capelo, Y. Zhang, J. Rodrigues, C. Liu, H. Tomas, Y. Li, P. He, Thermo/redox/pH-triple sensitive poly(N-isopropylacrylamide-co-acrylic acid) nanogels for anticancer drug delivery, J. Mater. Chem. B 3 (2015) 4221–4230.

[34] D. Mao, Q. Li, N. Bai, H. Dong, D. Li, Porous stable poly(lactic acid)/ethyl cellulose/hydroxyapatite composite scaffolds prepared by a combined method for bone regeneration, Carbohydr, Polym 180 (2018) 104–111.

[35] R. Elashnikov, P. Slepička, S. Rimpelova, P. Ulbrich, V. Švorčík, O. Lyutakov, Temperature-responsive PLLA/PNIPAM nanofibers for switchable release, Mater. Sci. Eng. C 72 (2017) 293–300.

[36] Y. Li, Y. Xiao, C. Liu, The horizon of materiobiology: a perspective on material-guided cell behaviors and tissue engineering, Chem. Rev. 117 (2017) 4376–4421.

[37] G. Jin, M.P. Prabhakaran, S. Ramakrishna, Stem cell differentiation to epidermal lineages on electrospun nanofibrous substrates for skin tissue engineering, Acta Biomater. 7 (2011) 3113–3122.

[38] N.D. Evans, E. Gentleman, The role of material structure and mechanical properties in cell-matrix interactions, J. Mater. Chem. B 2 (2014) 2345–2356.

[39] Y. Arima, H. Iwata, Effect of wettability and surface functional groups on protein adsorption and cell adhesion using well-defined mixed self-assembled monolayers, Biomaterials 28 (2007) 3074–3082.

[40] H.Y. Chang, C.C. Huang, K.Y. Lin, W.L. Kao, H.Y. Liao, Y.W. You, J.H. Lin, Y. T. Kuo, D.Y. Kuo, J.J. Shyue, Effect of surface potential on NIH3T3 cell adhesion and proliferation, J. Phys. Chem. C 118 (2014) 14464–14470.

[41] P. Saini, M. Arora, M.N.V.R. Kumar, Poly(lactic acid) blends in biomedical applications, Adv. Drug Deliv. Rev. 107 (2016) 47–59.

[42] K. Zhang, H. Zheng, S. Liang, C. Gao, Aligned PLLA nanofibrous scaffolds coated with graphene oxide for promoting neural cell growth, Acta Biomater. 37 (2016) 131–142.

[43] S.H. Oh, I.K. Park, J.M. Kim, J.H. Lee, In vitro and in vivo characteristics of PCL scaffolds with pore size gradient fabricated by a centrifugation method, Biomaterials 28 (2007) 1664–1671.

[44] C.S. Chen, M. Mrksich, S. Huang, G.M. Whitesides, D.E. Ingber, Geometric control of cell life and death, Science 276 (1997) 1425–1428.

[45] P.G. Rodriguez, F.N. Felix, D.T. Woodley, E.K. Shim, The role of oxygen in wound healing: a review of the literature, Dermatol. Surg. 34 (2008) 1159–1169.

[46] B. Ponugoti, F. Xu, C. Zhang, C. Tian, S. Pacios, D.T. Graves, FOXO1 promotes wound healing through the up-regulation of TGF-β1 and prevention of oxidative stress, J. Cell Biol. 203 (2013) 327–343.

[47] C. Dunnill, T. Patton, J. Brennan, J. Barrett, M. Dryden, J. Cooke, D. Leaper, N. T. Georgopoulos, Reactive oxygen species (ROS) and wound healing: the functional role of ROS and emerging ROS-modulating technologies for augmentation of the healing process, Int. Wound J. 14 (2017) 89–96.